ARTICLE

Depleted-Heterojunction Colloidal Quantum Dot Solar Cells

Andras G. Pattantyus-Abraham,[†,⊥] Illan J. Kramer,[†,⊥] Aaron R. Barkhouse,[†] Xihua Wang,[†] Gerasimos Konstantatos,[†,‡] Ratan Debnath,[†] Larissa Levina,[†] Ines Raabe,[§] Mohammad K. Nazeeruddin,[§] Michael Grätzel,[§] and Edward H. Sargent[†,*]

[†]Department of Electrical and Computer Engineering, University of Toronto, 10 King's College Road, Toronto, Ontario M5S 3G4, Canada, [‡]ICFO—Institut de Ciencies Fotoniques, Mediterranean Technology Park, 08860 Castelldefels, Barcelona, Spain, and [§]Laboratory for Photonics and Interfaces, Institute of Chemical Sciences and Engineering, School of Basic Sciences, Swiss Federal Institute of Technology, CH-1015 Lausanne, Switzerland. [⊥]These authors contributed equally to this work.

ABSTRACT Colloidal quantum dot (CQD) photovoltaics combine low-cost solution processability with quantum size-effect tunability to match absorption with the solar spectrum. Rapid recent advances in CQD photovoltaics have led to impressive 3.6% AM1.5 solar power conversion efficiencies. Two distinct device architectures and operating mechanisms have been advanced. The first—the Schottky device—was optimized and explained in terms of a depletion region driving electron–hole pair separation on the semiconductor side of a junction between an opaque low-work-function metal and a p-type CQD film. The second—the excitonic device—employed a CQD layer atop a transparent conductive oxide (TCO) and was explained in terms of diffusive exciton transport *via* energy transfer followed by exciton separation at the type-II heterointerface between the CQD film and the TCO. Here we fabricate CQD photovoltaic devices on TCOs and show that our devices rely on the establishment of a depletion region for field-driven charge transport and separation, and that they also exploit the large bandgap of the TCO to improve rectification and block undesired hole extraction. The resultant depleted-heterojunction solar cells provide a 5.1% AM1.5 power conversion efficiency. The devices employ infrared-bandgap size-effect-tuned PbS CQDs, enabling broadband harvesting of the solar spectrum. We report the highest open-circuit voltages observed in solid-state CQD solar cells to date, as well as fill factors approaching 60%, through the combination of efficient hole blocking (heterojunction) and very small minority carrier density (depletion) in the large-bandgap moiety.

KEYWORDS: quantum dot · solar cell · PbS · titanium dioxide · depleted heterojunction · exciton dissociation · electron transfer

Solar energy harvesting requires a combination of low cost and high efficiency in order to overcome balance-of-systems costs.[1] Solution-processing offers an attractive route to low cost per area of light-harvesting material; however, the materials must be carefully chosen to maximize the absorption of the sun's broad visible and infrared spectrum, and thus produce a high current density (J_{sc}) while maximizing the amount of work extracted from each absorbed photon *via* a large open-circuit voltage (V_{oc}) and fill factor (FF). The power conversion efficiency (η) for an input solar intensity (P_{solar}, typically 100 mW cm^{-2}) is given by

$$\eta = \frac{V_{oc} J_{sc} \mathrm{FF}}{P_{solar}}$$

Crystalline Si, which is a relatively weak light-absorber,[2] requires thick, high-purity solar cells with correspondingly long carrier transport lengths;[3] organic polymers, which absorb light very strongly, need a very thin distributed donor–acceptor heterojunction[4] to overcome a large exciton binding energy and low charge mobility.[5]

Here we introduce the device architecture and concepts that allow colloidal quantum dot (CQD) solar cells to achieve the joint optimization of V_{oc}, J_{sc}, and FF. We further present experimental validation of these concepts through the highest photovoltaic power conversion efficiencies reported in the CQD materials system.

Colloidal quantum dot photovoltaics[6,7] offer a widely tunable bandgap, enabling both optimal-bandgap solution-processed single-junction cells and also multijunction architectures. Size-effect tuning also enables the use of inexpensive, abundant ultralow-bandgap semiconductors otherwise unsuited for photovoltaic energy conversion.[8] CQD solar cell efficiencies have increased rapidly in recent years to 3.6% using the elegantly simple Schottky junction in combination with lead chalcogenides as the quantum-confined semiconductor.[9−16] These devices have harvested photons at wavelengths as long as 1800 nm, previously unachieved in a solution-processed device. Impressive short-circuit current densities reaching as high as 25 mA/cm² have been reported as a result.[9] Significant progress has also been achieved by sensitizing nanoporous TiO_2 electrodes with a thin layer of CQD[17−19]

*Address correspondence to ted.sargent@utoronto.ca.

Received for review February 18, 2010 and accepted May 12, 2010.

Published online May 24, 2010.
10.1021/nn100335g

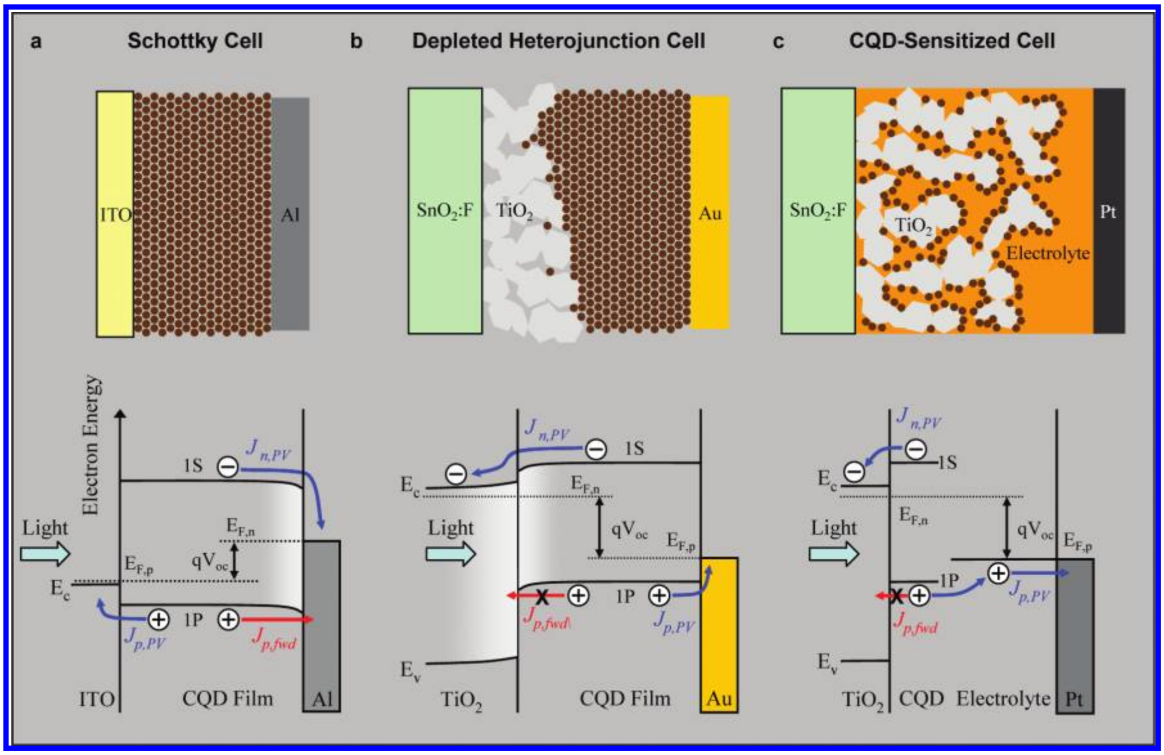

Figure 1. Comparison of three CQD photovoltaic architectures under photovoltaic operation close to maximum V_{oc}. (a) The Schottky design has lower FF and V_{oc} for a given J_{sc}, due to the poor barrier for hole injection into the electron-extracting contact. (b) The depleted heterojunction design combines the advantages of the other two cells, leading to simultaneously maximized FF, V_{oc}, and J_{sc}. (c) The CQD sensitized cell employs a thin layer of absorber on a high surface area electrode. The light-absorbing capacity of this design is lower, leading to poor J_{sc}, while it provides good FF and V_{oc}. $E_{F,n}$ and $E_{F,p}$ are the electron and hole quasi-Fermi levels; E_c and E_v are the conduction and valence band edges; $J_{p,PV}$ and $J_{n,PV}$ are the hole and electron photocurrents (and are equal at steady state); $J_{p,fwd}$ is the hole current in the forward bias direction.

(on the order of one monolayer; we term these CQD-sensitized solar cells, CQD-SSCs), where reported power conversion efficiencies have attained 3.2%.

The mechanisms that limit efficiency in these past reports can be readily recognized. For Schottky devices, both the V_{oc} and especially the FF have, to date, fallen well below their potential. As for CQD-SSC, significantly better V_{oc} and FF have been reported, but the J_{sc} values are generally lower.

Here we report a new solar cell architecture that overcomes the limitations of past CQD photovoltaics (PV). Our depleted-heterojunction (DH) device achieves FFs approaching 60%, compared to a previous CQD PV record[16] of 51%, and it achieves an open-circuit voltage of 0.53 V, compared to a previous CQD PV record of 0.45 V. The short-circuit current density reaches 16 mA cm^{-2} and exceeds those observed in CQD-SSC devices. Brought together, the optimized parameters allow our new architecture to reach an efficiency of 5.1% under AM1.5g illumination, compared to the best prior reports of 3.6%.[16]

We depict in Figure 1, and quantify in Table 1, the key conceptual issues that have limited previous CQD PV devices and the architectural advances that led to the performance improvement we report herein. The figure compares the Schottky barrier device architecture[20] with the DH-CQD device and the CQD-SSC. In the figure we employ spatial band diagrams to depict the behavior of CQD films in conjunction with metal contacts and heterojunctions with other semiconductors. Implied in these representations is an effective-medium

TABLE 1. CQD Solar Cell Figures of Merit for Different Device Architectures

reference	quantum dot (E_g)	model	V_{oc} (V)	J_{sc} (mA cm^{-2})	FF (%)	η (%)
this work	PbS (1.3 eV)	CQD-DH	0.51	16.2	58	5.1
	PbS (1.1 eV)	CQD-DH	0.45	13.2	35	2.1
	PbS (0.9 eV)	CQD-DH	0.38	11.3	21	0.93
Ma *et al.*	$PbS_{0.7}Se_{0.3}$ (1.0 eV)	CQD-Schottky	0.45	15	50	3.3
Debnath *et al.*	PbS (1.3 eV)	CQD-Schottky	0.51	14	51	3.6
Lee *et al.*	PbS (1.6 eV)	QD-SSC[a]	0.56	4.58	57	1.46
Giménez *et al.*	CdSe (2.0 eV)	CQD-SSC	0.51	7.1	48	1.83

[a]Quantum dots not colloidal but prepared by chemical bath deposition on the electrode; quantum confinement effects still evident.

picture of CQD solids, in which certain physical quantities of importance are averaged over regions of the nanostructured solid.[9,13,15,20] Such physical quantities include the variation of a built-in or applied field, the free carrier density, the net charge, the dielectric constant, and the quasi-Fermi-levels over a length scale considerably greater than the dot-to-dot separation. From this ansatz flow semiconductor device concepts such as the establishment of substantially depleted regions having a built-in field, and quasi-neutral regions in which minority carrier transport is dominated by diffusion. The mathematical underpinnings of this technique lie in the method of multiple scales: the quantum dot length scale determines bandstructure and transport properties, while averaged variations in carrier density, charge, field, and Fermi levels occur over considerably longer length scales.

Both the Schottky and the DH architectures show a depletion layer that arises from charge transfer from the electron-accepting contact to the p-type CQD film. Since metals have a very high free electron density[21] ($\sim 10^{22}$ cm^{-3}), there is a negligible depletion region on the metal side of the Schottky junction. In contrast, in the DH-CQD device, the TiO_2 electrode is partially depleted in view of its much lower $\sim 1 \times 10^{16}$ cm^{-3} n-type carrier density.

The Schottky device is disadvantaged by a number of factors. First, as light absorption begins at the ohmically contacted side, rather than the junction, many minority carriers (here electrons) must travel the thickness of the entire film before reaching their destination electrode and are therefore more susceptible to recombination. The DH design, with the transparent electron-accepting TiO_2 contact, benefits from minority carrier separation due to the placement of the junction on the illuminated side. Second, in the Schottky device, the open-circuit voltage is often limited by Fermi-level pinning due to defect states at the metal−semiconductor interface;[22] in contrast, the TiO_2−CQD interface may be passivated during the solution-phase deposition of the quantum dots. Third, the barrier to hole injection into the electron-extracting electrode of the Schottky device becomes much less effective when the device is operating in the photovoltaic quadrant. Both the DH and the CQD-SSC approaches mitigate this effect by introducing a large discontinuity in the valence band and by minimizing the electron density in the electron acceptor near the junction.

The CQD-SSC architecture can show good V_{oc} and FF since the electrolyte, whether solid or liquid, is usually a good hole transporter, and back-recombination of electrons and holes across the TiO_2−electrolyte interface can be blocked. However, a CQD monolayer adsorbed on the TiO_2 surface has a lower absorption coefficient than similarly created dye layers, and as such high J_{sc} values cannot be reached without compromising the FF. In contrast, the DH architecture can and indeed should employ many monolayers of the light-absorber due to the charge-transporting functionality of the CQD film.

We now turn to the specific instantiation of these concepts in our device and the detailed evidence in support of the advantages we propose. We built a heterojunction between a transparent TiO_2 electrode and an active layer consisting of PbS CQD with varying diameters. The energy level positions of these materials, consistent with multiple literature reports,[23,24] are shown in Figure 2, along with the solution absorption spectra. At the smallest size, 3.7 nm, the 1S electron excited state of the CQD lies well above (>0.3 eV) the TiO_2 conduction band level, and photoexcited electron injection into TiO_2 would be energetically favorable. The 1P hole level exhibits a large (>1.5 eV) discontinuity with the TiO_2 valence band, providing a very large barrier to the undesired passage of majority holes from the p-type CQD layer into the TiO_2 electrode. As the diameter of the CQD increases, the hole injection barrier is increased, while the driving force for electron transfer into TiO_2 diminishes, to the point of becoming negligible at a diameter of 5.5 nm. We note that the uncertainties in the energy levels are substantial ($\pm$0.1 eV), but the Fermi level differences act as a very good predictor for the experimentally observed V_{oc} (Figure 2b).

We built the light-absorbing semiconductor medium using layer-by-layer solution deposition of oleate-capped PbS CQD on TiO_2 electrodes, where each subsequent layer was treated using a solution of 3-mercaptopropionic acid in methanol. This treatment displaced the oleate ligand completely and rendered the CQD insoluble, which allowed 200 nm thick films to be created using 11 deposition cycles (Supporting Information). The device was then completed with a Au contact deposited through a shadow mask resulting in a device of area 0.05 cm^2. We were also able to build >1 cm^2 area devices - the rectifying nature of the TiO_2−Au junction helps to prevent electrical shorts at defects in the PbS CQD film. A cross-section of a typical device is shown in Figure 2c. Spatially resolved elemental analysis of the cross-section revealed very little interpenetration of the CQD and TiO_2 layers.

The photovoltaic response of the bandgap-tuned DH solar cells is reported in Figure 3a. It is striking that the short-circuit current remains comparable for all the CQD sizes studied. The largest CQD films considered in this study have a negligible conduction band offset relative to TiO_2, yet these 0.9 eV-quantum-confined-bandgap devices (diameter 5.5 nm) still showed a $\sim$10 mA/cm^2 (area 0.03 cm^2) short-circuit current and a V_{oc} of 0.38 V. These observations suggest that a large conduction band offset is not a requirement for efficient electron transfer from the PbS CQD into the TiO_2 electrode. The results are encouraging for the realization of highly efficient devices, as the requirement of a large band offset between the electron donor and acceptor can im-

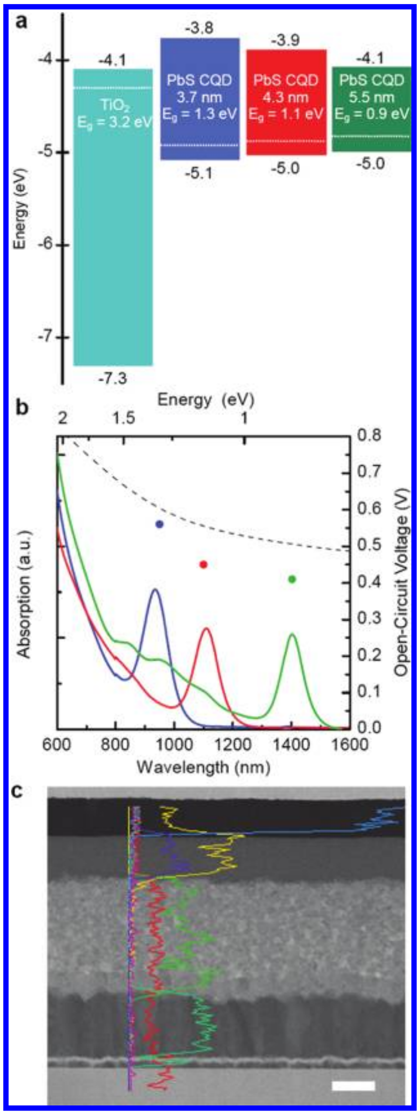

Figure 2. (a) Energy level alignment of TiO_2 and PbS CQD (1S, the first electronic excited state; 1P, the first excited hole state) of different sizes. The Fermi level is shown as a dashed line for $\sim 10^{16}$ cm^{-3} n-type doping in TiO_2 and $\sim 2 \times 10^{16}$ cm^{-3} doping in PbS CQD. (b) Solution absorption spectra in toluene of the three different PbS CQD sizes used in device fabrication. The experimental V_{oc} values are shown above each excitonic peak, and the upper limit to V_{oc}, calculated from the difference in Fermi levels shown in panel (a), is shown as a dashed line. (c) Cross-sectional TEM of a photovoltaic device. The sample was prepared by focused-ion-beam milling. The line plot shows the elemental distribution as determined by energy-dispersive X-ray analysis (yellow, S; blue, Pb; green, Ti; cyan, Sn; red, O; light blue, Au). The scale bar is 200 nm.

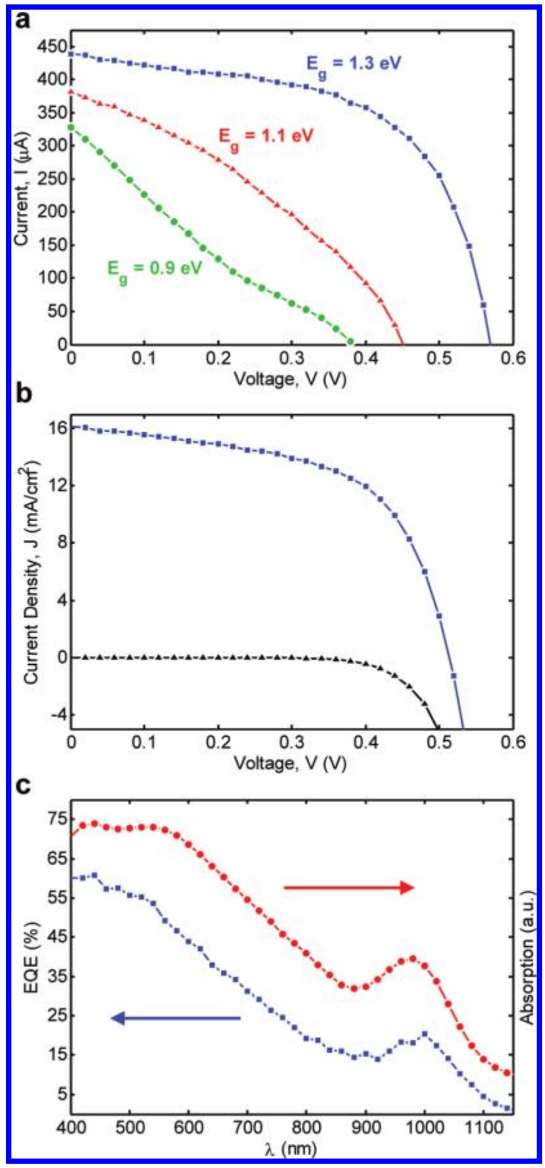

Figure 3. (a) Unapertured I−V response of FTO/porous TiO_2/PbS QD/Au photovoltaic devices from three different CQD sizes (device area 0.03 cm^2). (b) Apertured dark and illuminated J-V curves for the champion device yielding short-circuit current of 16.2 mA/cm^2, open-circuit voltage of 0.51 V, fill factor of 58% and PCE of 5.1% under 94% of one sun illumination. Here the device had a 0.06 cm^2 contact area that was apertured down to a 0.05 cm^2 device area to eliminate any lateral collection of photogenerated carriers. (c) Apertured external quantum efficiency and absorption spectra for a champion device based on PbS CQDs having a bandgap of 1.3 eV ($\sim$960 nm first excitonic peak).

pose a substantial efficiency penalty. In organic photovoltaics this appears as a lower-than-desired open-circuit voltage.[25,26] Furthermore, a wide range of junctions should be achievable using a generalization of this approach; it follows that multijunction devices can then be realized within a single materials-processing architecture.

We also note that the photocurrents in the DH devices conflict with the conclusions drawn from previous photoluminescence quenching experiments[23] where it was suggested that only PbS CQD with a bandgap larger than 1 eV could transfer electrons to TiO_2 particles in solution. This suggests that electron back-transfer from TiO_2 to the PbS CQD in the DH architecture is strongly suppressed by the built-in field of the depletion region.

We now focus on the performance of our best devices. These were chosen to have a near-optimal single-junction bandgap of 1.3 eV (diameter 3.7 nm), and we report here the average parameters of five representative devices, as well champion device performance. The representative devices showed a V_{oc} of 0.53 ± 0.02 V, a J_{sc} of 15.3 ± 1.2 mA cm^{-2} and a FF of 57 ± 4%. The average AM1.5 power conversion efficiency was η = 4.9 ± 0.3%. The best device parameters were V_{oc} = 0.51 V, J_{sc} = 16.2 mA cm^{-2} and FF = 58%, yielding η = 5.1%. Figure 3b shows the J-V performance for this champion 1.3 eV bandgap PbS QD solar cell. We also fabricated large-area devices (area 1.05 cm^2) and obtained the same J_{sc} > 15 mA cm^{-2} for the large contacts as for the smaller ones.

We report in Figure 3c the external quantum efficiency spectrum, the ratio of extracted electrons to incident photons as a function of wavelength (also known as IPCE, the incident photon conversion efficiency spectrum). At short wavelengths, the EQE reaches 60%. Photons at these wavelengths are converted and extracted more efficiently as light is absorbed closer to the TiO_2 interface.[27] At longer wavelengths, the distinctive excitonic feature can be resolved and at its peak the EQE is 20%. For comparison we include the absorption curve for this device in the same figure.

We integrated the product of the measured EQE spectrum with the AM 1.5 solar simulator spectrum and obtained 15 ± 1 mA cm^{-2} for the representative devices. These values agree, within measurement error, with those obtained directly using our solar simulator. This further confirms that there is no decrease in the EQE spectrum under higher illumination intensities, which is consistent with our high fill factor at solar intensities.

Our good fill factors are further explicated through studying the variation of device capacitance with bias (Figure 4a). This capacitance arises from the depletion layer due to charge transfer from TiO_2 to the PbS CQD layer. The capacitance, and its associated depletion layer distributed between the two semiconductors, peaks at a bias of 0.52 V. This value of built-in potential agrees well with the observed open-circuit voltage. This is a direct signature of the presence of a built-in field that can efficiently drive the separation of photogenerated carriers.

This observed built-in potential is in turn explainable from the Fermi level difference between the n-type TiO_2 and the p-type PbS CQD film. To estimate the doping in the CQD we built a device for further Mott−Schottky analysis[28] employing instead a heavily n-doped compact TiO_2 electrode.[29] The result is in Figure 4b. The reverse-biased capacitance is used to estimate the permittivity of the PbS CQD layer based on its 200 ± 20 nm thickness measured by scanning electron microscopy. The relative permittivity is thereby calculated to be ϵ_r = 43 ± 4. The slope of A^2/C^2 vs V in the linear regime was 1.7×10^6 m^4 F^{-2} V^{-1}, from which the net doping density in the PbS CQD film is found to be ~2×10^{16} cm^{-3}. Combining this information with

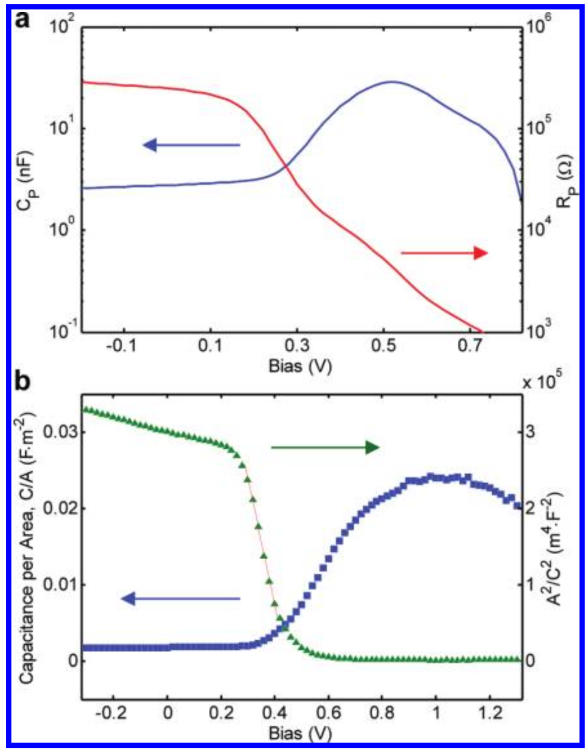

Figure 4. Capacitance−voltage curves of (a) the champion TiO_2/1.3 eV QD PV/Au device. The impedance was acquired at 1 kHz with a signal amplitude of 10 mV, and is represented here in terms of equivalent parallel resistance (R_p) and capacitance (C_p) for a device with contact area of 0.06 cm^2. (b) a FTO/compact TiO_2/1.3 eV PbS QD/Au structure. Mott−Schottky analysis was performed to arrive at approximate values for free carriers in 1.3 eV PbS QD films.

size-dependent HOMO levels[23] we estimate the Fermi level to lie:

− 4.9 ± 0.1 eV below vacuum for 3.7 nm (λ_{ex} = 950 nm) PbS CQDs; and

− 4.8 eV ± 0.1 eV below vacuum for 5.5 nm (λ_{ex} = 1400 nm) PbS QDs.

Literature values for doping density in nanoporous TiO_2 start at $n = 1 \times 10^{16}$ cm^{-3}.[30−32] From published bandedge information for TiO_2 of E_{CB} = 4.1 ± 0.1 eV, we estimate that the Fermi level lies 4.3 ± 0.1 eV below vacuum.

We conclude that the built-in potential for the smaller-dot devices of 0.53 V, and also the somewhat lower values for the larger-dot devices, can be explained entirely from the Fermi level (semiconductor work function) difference across the N-p junction.

We now discuss in greater detail the chemical composition of our MPA-capped PbS QD films. Figure 5a shows the infrared transmittance spectra of pure MPA as well as MPA-capped PbS QD films. Of note is the relative intensity of the unbound carboxylic acid band at ~1703 cm^{-1}, and the Pb-bound carboxylate band at ~1500 cm^{-1}. This suggests that a substantial fraction of MPA ligands are bound in bidentate fashion to the PbS quantum dot surface. This type of bidentate binding of MPA to Pb^{2+} has been reported previously.[33]

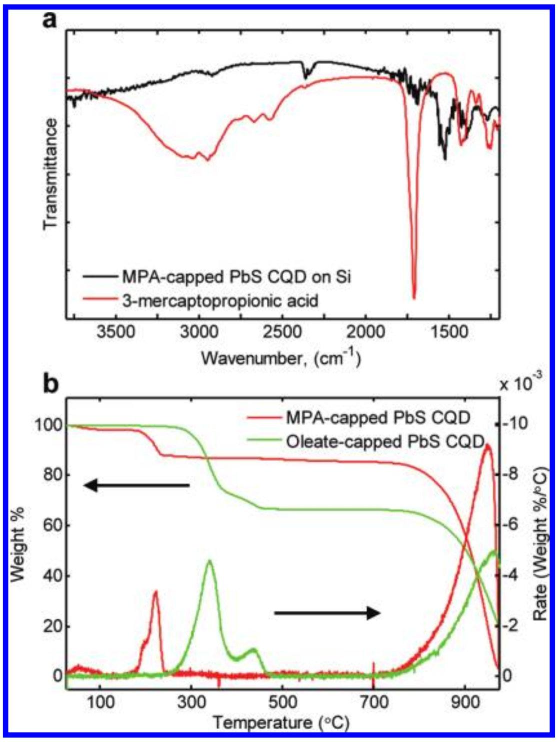

Figure 5. (a) Infrared transmission spectra of 3-mercaptopropionic acid (MPA) and MPA-capped PbS QD films on silicon. (b) Thermogravimetric analysis of PbS QD under N_2.

The thermal stability of MPA-capped PbS CQD is also of great importance in photovoltaic device processing and use. Figure 5b shows the thermogravimetric analysis under N_2 (heating rate 10 °C min^{-1}). No significant mass loss occurs below 150 °C and a peak loss rate arises at 220 °C. These temperatures are both well above the boiling point of MPA (~110 °C) providing a further indication that MPA is strongly bound to the PbS surface.

We conclude with a discussion of the nature of charge and energy transport within CQD films and of the importance of these insights in the design of high-performance CQD PV devices. Recent reports[11,12] have described energy transport in CQD PV devices as excitonic: bound electron–hole pairs diffuse, through Förster transfer, to a charge-separating heterojunction. This has led to the study of very thin devices (~50 nm thick),[11] which severely curtails the potential for high J_{sc} in planar device due to finite optical absorption coefficients (10^4 to 10^5 cm^{-1}). Semiconducting materials with strongly bound excitons are more naturally optimized in a different framework than the DH architecture (*e.g.*, the CQD-SSC or bulk heterojunction approach).

For the PbS CQD (E_g ~ 1.3 eV) used in our devices, the time for Förster transfer from one dot to its neighbor are estimated to be in the range of 200 to 400 ns.[34] The exciton radiative lifetime is 1–2 μs.[34,35] in these materials. One would therefore expect efficient Förster transfer only over a few dot-to-dot transfers. However our optimal devices have 200–250-nm-thick light-absorbing regions and exhibit high internal and external quantum efficiencies. Förster transfer cannot account for efficient transport over the >~ 50 hops over which charge carriers successfully transit our most efficient devices.

We conclude that transport in these CQD films is best understood through the rapid dissociation of excitons in the presence of a built-in field, followed by drift and diffusion of electrons and holes. The validity of these concepts has been demonstrated elsewhere experimentally[36] and is borne out in the beneficial impact of implementing the DH architecture.

METHODS

PbS CQDs were synthesized using a variation on a literature method.[37] TiO_2 electrodes were prepared from a commercially available TiO_2 paste (DSL-90T, Dyesol, Inc.) on SnO_2:F-coated glass substrates (Pilkington TEC 15, Hartford Glass, Inc.). No compact TiO_2 was employed except where explicitly stated. Quantum dot films were prepared on TiO_2 electrodes by multilayer spincoating of 37.5 mg mL^{-1} solution in a 3:1 mixture of octane:decane under ambient conditions. Each layer was deposited at 2500 rpm and treated briefly with 10 vol % 3-mercaptopropionic acid in methanol also spin-cast at 2500 rpm; each layer was then rinsed with methanol and octane while spinning at 2500 rpm. The device was then transferred to a glovebox with N_2 atmosphere and left overnight. Gold contacts, 15 nm thick, were deposited by thermal evaporation at a rate of 0.4 Å/s at a pressure of $<1 \times 10^{-6}$ mbar. Contact sizes were 0.061 cm^2.

J-V data was measured using a Keithley 2400 source-meter in N_2 environment. The solar spectrum at AM1.5 was simulated to within class A specifications (less than 25% spectral mismatch) with a Xe lamp and filters (Solar Light Company Inc.) with measured intensity at 94 mW cm^{-2}. The source intensity was measured with a Melles-Griot broadband power meter (responsive from 300 to 2000 nm), through a circular 0.049 cm^2 aperture at the position of the sample and confirmed with a calibrated solar cell (Newport, Inc.). The accuracy of the power measurements was estimated to be ±7%.

The external quantum efficiency spectrum was obtained by passing the output of a 400W Xe lamp through a monochromator and using appropriate order-sorting filters. The collimated output of the monochromator was measured through a 1 mm aperture with calibrated Newport 818-UV and Newport 818-IR power meters as needed. The measurement bandwidth was ~40 nm and the intensity varied with the spectrum of the Xe lamp. The average intensity was 1.7 mW cm^{-2}. The current–voltage response was measured with Keithley 2400 source-meters.

Capacitance–voltage measurements were performed directly on the photovoltaic devices using an Agilent 4284A LCR meter. Absorption spectroscopy was carried out on a Cary 500 UV–vis–IR Scan photospectrometer. Transmission electron microscopy and spatially resolved X-ray elemental analysis was performed on a thin section sample prepared by focused-ion-beam milling (Material Science Services Corp.).

Acknowledgment. This research was supported by Award No. KUS-I1-009-21, made by King Abdullah University of Science and Technology (KAUST). The authors also acknowledge the assistance of L. Brzozowski, S. Huang, K. Kemp, G. Koleilat, J. Tang, E. Palmiano, R. Wolowiec, and D. Jamaskosmanovic. M.G. and M.K.N. thank the Korea Foundation for International Coop-

ARTICLE

eration of Science and Technology through the Global Research Laboratory (GRL) Program funded by the Ministry of Education, Science and Technology, Republic of Korea.

Supporting Information Available: Detailed list of chemicals used, methods for synthesis and purification of PbS CQDs, methods for preparing porous TiO_2 electrodes, and methods for preparing PbS CQD films using a layer-by-layer technique. This material is available free of charge *via* the Internet at http://pubs.acs.org.

REFERENCES AND NOTES

1. Raugei, M.; Frankl, P. In *Sustainable Energy Production and Consumption*; 2008; pp 293−304.
2. Adachi, S. In *Handbook on physical properties of semiconductors*; Springer, 2004; Vol. 1, p 93.
3. Luque, A.; Hegedus, S. In *Handbook of photovoltaic science and engineering*; John Wiley and Sons, 2003; p 193.
4. Yu, G.; Gao, J.; Hummelen, J. C.; Wudl, F.; Heeger, A. J. Polymer Photovoltaic Cells: Enhanced Efficiencies via a Network of Internal Donor-Acceptor Heterojunctions. *Science* **1995**, *270*, 1789–1791.
5. Günes, S.; Neugebauer, H.; Sariciftci, N. S. Conjugated Polymer-Based Organic Solar Cells. *Chem. Rev.* **2007**, *107*, 1324–1338.
6. Sargent, E. H. Infrared Photovoltaics Made by Solution Processing. *Nat. Photon.* **2009**, *3*, 325–331.
7. Hillhouse, H. W.; Beard, M. C. Solar Cells from Colloidal Nanocrystals: Fundamentals, Materials, Devices, and Economics. *Curr. Opin. Colloid Interface Sci.* **2009**, *14*, 245–259.
8. Wadia, C.; Alivisatos, A. P.; Kammen, D. M. Materials Availability Expands the Opportunity for Large-Scale Photovoltaics Deployment. *Environ. Sci. Technol.* **2009**, *43*, 2072–2077.
9. Luther, J. M.; Law, M.; Beard, M. C.; Song, Q.; Reese, M. O.; Ellingson, R. J.; Nozik, A. J. Schottky Solar Cells Based on Colloidal Nanocrystal Films. *Nano Lett.* **2008**, *8*, 3488–3492.
10. Ma, W.; Luther, J. M.; Zheng, H.; Wu, Y.; Alivisatos, A. P. Photovoltaic Devices Employing Ternary PbS_xSe_{1-x} Nanocrystals. *Nano Lett.* **2009**, *9*, 1699–1703.
11. Choi, J. J; Lim, Y; Santiago-Berrios, M. B; Oh, M; Hyun, B; Sun, L; Bartnik, A. C; Goedhart, A; Malliaras, G. G; Abruña, H. D; Wise, F. W; Hanrath, T. PbSe Nanocrystal Excitonic Solar Cells. *Nano Lett.* **2009**, *9*, 3749–3755.
12. Leschkies, K. S.; Beatty, T. J.; Kang, M. S.; Norris, D. J.; Aydil, E. S. Solar Cells Based on Junctions between Colloidal PbSe Nanocrystals and Thin ZnO Films. *ACS Nano* **2009**, *3*, 3638–3648.
13. Johnston, K. W.; Pattantyus-Abraham, A. G.; Clifford, J. P.; Myrskog, S. H.; MacNeil, D. D.; Levina, L.; Sargent, E. H. Schottky-Quantum Dot Photovoltaics for Efficient Infrared Power Conversion. *Appl. Phys. Lett.* **2008**, *92*, 151115.
14. Klem, E. J. D.; MacNeil, D. D.; Cyr, P. W.; Levina, L.; Sargent, E. H. Efficient Solution-Processed Infrared Photovoltaic Cells: Planarized All-Inorganic Bulk Heterojunction Devices via Inter-Quantum-Dot Bridging during Growth from Solution. *Appl. Phys. Lett.* **2007**, *90*, 183113.
15. Koleilat, G. I.; Levina, L.; Shukla, H.; Myrskog, S. H.; Hinds, S.; Pattantyus-Abraham, A. G.; Sargent, E. H. Efficient, Stable Infrared Photovoltaics Based on Solution-Cast Colloidal Quantum Dots. *ACS Nano* **2008**, *2*, 833–840.
16. Debnath, R.; Tang, J.; Barkhouse, D. A.; Wang, X.; Pattantyus-Abraham, A. G.; Brzozowski, L.; Levina, L.; Sargent, E. H. Ambient-Processed Colloidal Quantum Dot Solar Cells via Individual Pre-Encapsulation of Nanoparticles. *J. Am. Chem. Soc.* **2010**, *132*, 5952–5953.
17. Fan, S.; Kim, D.; Kim, J.; Jung, D. W.; Kang, S. O.; Ko, J. Highly Efficient CdSe Quantum-Dot-Sensitized TiO_2 Photoelectrodes for Solar Cell Applications. *Electrochem. Commun.* **2009**, *11*, 1337–1339.
18. Lee, H.; Leventis, H. C.; Moon, S.; Chen, P.; Ito, S.; Haque, S. A.; Torres, T.; Nüesch, F.; Geiger, T.; Zakeeruddin, S. M.; Grätzel, M.; Nazeeruddin, M. K. PbS and CdS Quantum Dot-Sensitized Solid-State Solar Cells: "Old Concepts, New Results". *Adv. Funct. Mater.* **2009**, *19*, 2735–2742.
19. Giménez, S.; Mora-Sero, I.; Macor, L.; Guijarro, N.; Lana-Villarreal, T.; Gomez, R.; Diguna, L. J.; Shen, Q.; Toyoda, T.; Bisquert, J. Improving the Performance of Colloidal Quantum-Dot-Sensitized Solar Cells. *Nanotechnology* **2009**, *20*, 295204.
20. Clifford, J. P.; Johnston, K. W.; Levina, L.; Sargent, E. H. Schottky Barriers to Colloidal Quantum Dot Films. *Appl. Phys. Lett.* **2007**, *91*, 253117.
21. Ashcroft, N. W.; Mermin, N. D. *Solid State Physics*; Saunders College, 1976.
22. Mönch, W. In *Semiconductor surfaces and interfaces*; Springer, 2001; p 572.
23. Hyun, B.; Zhong, Y.; Bartnik, A. C.; Sun, L.; Abruña, H. D.; Wise, F. W.; Goodreau, J. D.; Matthews, J. R.; Leslie, T. M.; Borrelli, N. F. Electron Injection from Colloidal PbS Quantum Dots into Titanium Dioxide Nanoparticles. *ACS Nano* **2008**, *2*, 2206–2212.
24. Dissanayake, D. M. N. M.; Lutz, T.; Curry, R. J.; Silva, S. R. P. Measurement and Validation of PbS Nanocrystal Energy Levels. *Appl. Phys. Lett.* **2008**, *93*, 043501-3.
25. Scharber, M. C.; Mühlbacher, D.; Koppe, M.; Denk, P.; Waldauf, C.; Heeger, A.; Brabec, C. Design Rules for Donors in Bulk-Heterojunction Solar Cells—Towards 10 % Energy-Conversion Efficiency. *Adv. Mater.* **2006**, *18*, 789–794.
26. Coakley, K. M.; McGehee, M. D. Conjugated Polymer Photovoltaic Cells. *Chem. Mater.* **2004**, *16*, 4533–4542.
27. Law, M.; Beard, M. C.; Choi, S.; Luther, J. M.; Hanna, M. C.; Nozik, A. J. Determining the Internal Quantum Efficiency of PbSe Nanocrystal Solar Cells with the Aid of an Optical Model. *Nano Lett.* **2008**, *8*, 3904–3910.
28. Schottky, W. Vereinfachte und Erweiterte Theorie der Randschicht-Gleichrichter. *Z. Phys.* **1942**, *118*, 539–592.
29. Kavan, L.; Grätzel, M. Highly Efficient Semiconducting TiO_2 Photoelectrodes Prepared by Aerosol Pyrolysis. *Electrochim. Acta* **1995**, *40*, 643–652.
30. O'Regan, B.; Moser, J.; Anderson, M.; Graetzel, M. Vectorial Electron Injection into Transparent Semiconductor Membranes and Electric Field Effects on the Dynamics of Light-Induced Charge Separation. *J. Phys. Chem.* **1990**, *94*, 8720–8726.
31. Nakade, S.; Saito, Y.; Kubo, W.; Kanzaki, T.; Kitamura, T.; Wada, Y.; Yanagida, S. Enhancement of Electron Transport in Nano-Porous TiO_2 Electrodes by Dye Adsorption. *Electrochem. Commun.* **2003**, *5*, 804–808.
32. Zaban, A.; Meier, A.; Gregg, B. A. Electric Potential Distribution and Short-Range Screening in Nanoporous TiO_2 Electrodes. *J. Phys. Chem. B* **1997**, *101*, 7985–7990.
33. Shindo, H.; Brown, T. L. Infrared Spectra of Complexes of L-Cysteine and Related Compounds with Zinc(II), Cadmium(II), Mercury(II), and Lead(II). *J. Am. Chem. Soc.* **1965**, *87*, 1904–1909.
34. Clark, S.; Harbold, J.; Wise, F. Resonant Energy Transfer in PbS Quantum Dots. *J. Phys. Chem. C* **2007**, *111*, 7302–7305.
35. Warner, J. H.; Thomsen, E.; Watt, A. R.; Heckenberg, N. R.; Rubinsztein-Dunlop, H. Time-Resolved Photoluminescence Spectroscopy of Ligand-Capped Pbs Nanocrystals. *Nanotechnology* **2005**, *16*, 175–179.
36. Choi, J. J.; Luria, J.; Hyun, B.; Bartnik, A. C.; Sun, L.; Lim, Y.; Marohn, J. A.; Wise, F. W.; Hanrath, T. Photogenerated Exciton Dissociation in Highly Coupled Lead Salt Nanocrystal Assemblies. *Nano Lett.* **2010**, 1805–1811.
37. Hines, M.; Scholes, G. Colloidal PbS Nanocrystals with Size-Tunable Near-Infrared Emission: Observation of Post-Synthesis Self-Narrowing of the Particle Size Distribution. *Adv. Mater.* **2003**, *15*, 1844–1849.